Stable monolayer honeycomb-like structures of RuX_2 (X = S, Se)

Fatih Ersan,[1] Seymur Cahangirov,[2] Gökhan Gökoğlu,[3] Angel Rubio,[4,5,*] and Ethem Aktürk[1,6,†]

[1]*Department of Physics, Adnan Menderes University, Aydın 09010, Turkey*

[2]*UNAM-Institute of Materials Science and Nanotechnology, Bilkent University, Ankara 06800, Turkey*

[3]*Department of Physics, Karabük University, 78050 Karabük, Turkey*

[4]*Max Planck Institute for the Structure and Dynamics of Matter, Luruper Chaussee 149, 22761 Hamburg, Germany*

[5]*Nano-Bio Spectroscopy Group and ETSF, Dpto. Fisica de Materiales, Universidad del País Vasco, 20018 San Sebastián, Spain*

[6]*Nanotechnology Application and Research Center, Adnan Menderes University, Aydın 09010, Turkey*

(Received 22 July 2016; published 11 October 2016)

Recent studies show that several metal oxides and dichalcogenides (MX_2), which exist in nature, can be stable in two-dimensional (2D) form and each year several new MX_2 structures are explored. The unstable structures in H (hexagonal) or T (octahedral) forms can be stabilized through Peierls distortion. In this paper, we propose new 2D forms of RuS_2 and $RuSe_2$ materials. We investigate in detail the stability, electronic, magnetic, optical, and thermodynamic properties of 2D RuX_2 (X = S, Se) structures from first principles. While their H and T structures are unstable, the distorted T structures (T'-RuX_2) are stable and have a nonmagnetic semiconducting ground state. The molecular dynamic simulations also confirm that T'-RuX_2 systems are stable even at 500 K without any structural deformation. T'-RuS_2 and T'-$RuSe_2$ have indirect band gaps with 0.745 eV (1.694 eV with HSE) and 0.798 eV (1.675 eV with HSE) gap values, respectively. We also examine their bilayer and trilayer forms and find direct and smaller band gaps. We find that AA stacking is more favorable than the AB configuration. The new 2D materials obtained can be good candidates with striking properties for applications in semiconductor electronic, optoelectronic devices, and sensor technology.

DOI: 10.1103/PhysRevB.94.155415

I. INTRODUCTION

Because of the quantum and surface effects, two-dimensional (2D) or quasi-2D materials have unique physical properties and are more effective in low-dimensional technology compared with their three-dimensional (3D) forms. The best example of this phenomenon is the graphite and its single atomic plane; namely, graphene. The former shows semimetallic behavior with ∼41 meV band overlap, while latter is a zero-gap semiconductor with various striking properties [1,2]. Similar to graphene; silicene [3], boron nitride (BN) [4–6], and zinc oxide (ZnO) [7,8] have attracted great interest due to their novel properties which are not observed in their bulk structures. Nowadays, the other attractive subjects are transition-metal dichalcogenides (TMDs) and transition-metal oxides (TMOs) layers [9–15]. The chemical composition of these materials is MX_2, where M is a transition metal and X is an O, S, Se, or Te atom. Generally, TMD and TMO groups have an intrinsic band gap in the range of 1–2 eV [16–18]. This property puts them one step forward in field-effect transistors and optoelectronic devices compared with graphene-based devices. While many MX_2 bulk structures have an indirect band gap, their single layers demonstrate direct band gaps and also they have enhanced photoluminescence and valley polarization properties [14,18–21].

Several band-gap-engineering studies show that the electronic band gap can be tuned by applying strain on the material. Among them, TMDs have high Young's modulus, so they are appropriate for strong and flexible electronics applications [22]. In recent years, researchers have explored multitudinous new 2D materials experimentally and theoretically. By using a first principles approach, Ataca *et al.* studied the stability of single layer 3d transition metals from Sc to Ni in MX_2 form [12]. Tongay *et al.* proved that $ReSe_2$ exhibits monolayer behavior in bulk $ReSe_2$ due to the electronic and vibrational decoupling, while electronic bands of $ReSe_2$ remain as direct gap from bulk to monolayer structure [14]. WSe_2, $TaSe_2$, and TaS_2 structures were obtained by mechanical exfoliation [23]. Chhowalla *et al.* prepared transition-metal dichalcogenide nanosheets by liquid exfoliation and by chemical vapor deposition [24]. Recently, Heine *et al.* showed that PdS_2 shows semiconducting properties in monolayer form, while it is semimetallic as a bilayer [25].

Very interestingly, we did not encounter any study about ruthenium (Ru) layers in MX_2 form despite of its fascinating properties. While Ru is a poor catalyst at low pressure [26], it can show high catalytic properties in excess O_2 at atmospheric pressure [27,28]. RuS_2 is very important for thermal catalytic processing of nitrogen compounds in petroleum refinement and it also has interesting photochemical catalytic properties [29,30]. A $RuSe_2$ system was discussed in several studies to investigate its photoacoustic characterization, thermodynamic, electronic, and electrocatalytic properties for the oxygen reduction reaction [31].

Due to the information mentioned above, we carried out a systematic study of RuS_2 and $RuSe_2$ based on first-principles density functional theory calculations. On the basis of extensive analysis of stability, we determined that two-dimensional forms of RuS_2 and $RuSe_2$ are found to be stable.

II. COMPUTATIONAL METHODS

First-principles plane-wave calculations within density functional theory (DFT) are carried out by using the

*angel.rubio@ehu.es

†ethem.akturk@adu.edu.tr

projector-augmented wave (PAW) potential method [32] as implemented in the Vienna *ab initio* simulation package (VASP) software [33]. The exchange-correlation interaction is treated by using the generalized gradient approximation (GGA) in the Perdew–Burke–Ernzerhof (PBE) form [34] for both spin-polarized and spin-unpolarized cases. A plane-wave basis set with kinetic energy cutoff of 400 eV is used for all the calculations. The vacuum spacing between the image surfaces due to the periodic boundary condition is kept larger than 25 Å. By using the conjugate gradient method, all atomic positions and lattice vectors in all structures are fully optimized until all the Hellmann–Feynman forces on each atom are less than 0.001 eV/Å and the total energy difference between two successive steps is smaller than 10^{-5} eV. The pressure in the unit cell is kept below ∼0.5 kbar. In addition to full optimization, we also calculate phonon dispersion curves by using the finite displacement method (FDM) [35]. The real values of vibrational mode frequencies over the whole Brillouin zone (BZ) is regarded as a critical indication of the structural stability. Brillouin zone integration is realized by a $(15 \times 15 \times 1)$ special k-point mesh for monolayer H and T structures and $(7 \times 15 \times 1)$ mesh for T′-RuX_2 cells following the convention of Monkhorst–Pack [36]. To get more accurate results, we also perform band dispersion calculations by the Heyd–Scuseria–Ernzerhof (HSE) hybrid functional [37–39]. The screening length of HSE is 0.2 Å^{-1}, and the mixing rate of the HF exchange potential is 0.25. For bilayer and trilayer structures, the calculations are performed with van der Waals correction [40].

III. RESULTS AND DISCUSSIONS

The 3D forms of both RuS_2 and $RuSe_2$ systems crystallize in cubic pyrite structure with $Pa3$ space group which is different from most of the TMD systems. The structural parameters, crystallographic configuration, and electronic band structures of bulk RuX_2 systems are given in the Supplemental Material [41]. Figure 1 illustrates the top view of H-, T-, and T'-RuX_2 unit cells together with side and top views of expanded RuX_2 structures below them. Our calculations show that the hexagonal (H) and octahedral (T) phases of RuX_2 structures are unstable due to having imaginary phonon frequencies. Upon the Peierls distortion the T phase is transformed into the distorted T phase; labeled as T'-RuX_2 [14,42,43]. These T' structures include two Ru and four X atoms in orthorhombic unit cell (i.e., rectangular in 2D projection). Our structures form chains similar to the ones observed in other T' structures including ReS_2 [14], MoS_2 [42], and $MoTe_2$ [43]. This may occur due to the similarity of the electronegativities of Ru (2.20), Mo (2.16), and Re (1.90) atoms. These MX quasi-1D chains (M is the metal and X is the chalcogen) are the manifestation of the Peierls distortion [44].

We choose orthorhombic cells to construct T' structures with fixed $c = 25$ Å lattice vector. Other two lattice vectors are determined as follows: $a = 5.561$ Å, $b = 3.450$ Å for RuS_2 and $a = 5.789$ Å, $b = 3.597$ Å for $RuSe_2$. These increments in lattice constants conform to atomic radii and electronegativities of X atoms, according to Pauli scale; S (2.58), and Se (2.55). The bonds between Ru and X atoms have covalent character compatible with the electronegativities. To determine the strength of cohesion between the atoms, we calculate the cohesive energy per RuX_2 unit by using the following equation:

$$E_{\text{Coh}} = [E_{\text{Ru}} + 2E_X - E_{\text{Ru}X_2}]/2, \quad (1)$$

where E_{Ru} and E_X are the total energies of free Ru and X atoms, $E_{\text{Ru}X_2}$ is the total energy of the RuX_2 structure. We estimate the cohesive energies to be 14.279 and 13.189 eV per RuX_2 formula unit for T'-RuS_2 and T'-$RuSe_2$ systems, respectively. These values are larger than that of T-RuX_2 forms and indicate strong cohesion between the constituent atoms. The larger cohesive energies indicate that T' states are energetically more favorable. Table I includes the optimized lattice constants and other equilibrium parameters of RuX_2 systems for T and T' phases. The additional crystallographic data including bond lengths and angles are also given in the Supplemental material [41].

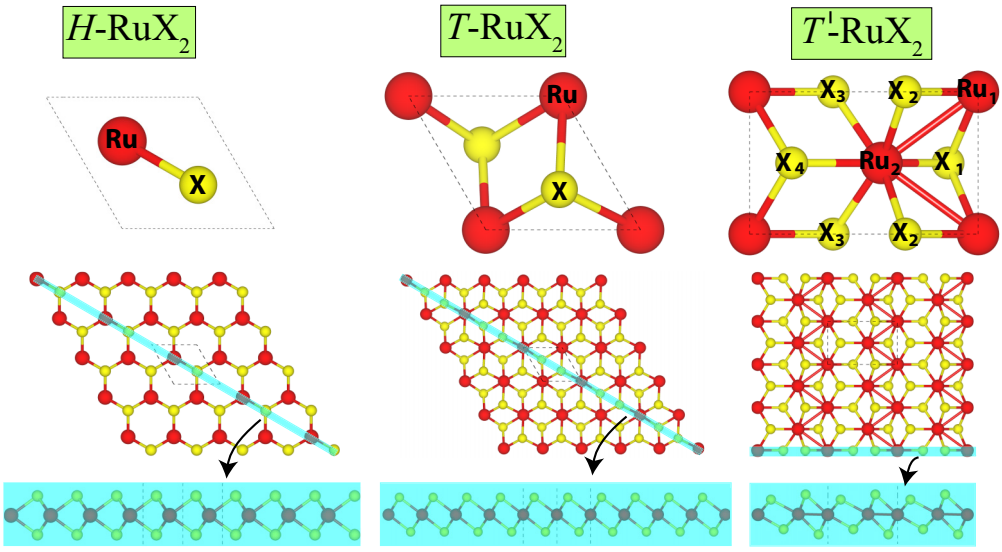

FIG. 1. The primitive cell and the top and side views of H-, T-, and T'-RuX_2 structures.

TABLE I. The equilibrium optimized structural parameters of RuX_2 (X = S, Se) systems in T and T' forms: lattice constants, cohesive and band-gap energies, magnetic moment, charge differences (according to Bader [45] analysis), Poisson's ratio, and in-plane stiffness [46].

System	Lattice (Å)	E_{coh} (eV)	E_g (eV)	μ (μ_B)	ρ (electrons)	ν_{xy}/ν_{yx}	C_x/C_y (J/m^2)
T-RuS_2	$a = b = 3.338$	13.544	metal	1.77	$Ru = -1.00$ $S = +0.50$		
T-$RuSe_2$	$a = b = 3.475$	12.455	metal	1.48	Ru $= -0.60$ Se $= +0.30$		
T'-RuS_2	$a = 5.561$ $b = 3.450$	14.279	0.745 PBE 1.694 HSE	0	$Ru_1 = -0.90$ $Ru_2 = -0.93$ $S_{all} = +0.46$	0.295/0.292	99/98
T'-$RuSe_2$	$a = 5.789$ $b = 3.597$	13.189	0.798 PBE 1.675 HSE	0	$Ru_1 = -0.54$ $Ru_2 = -0.58$ $S_{all} = +0.29$	0.300/0.286	85/81

To check the dynamical stability of the proposed structures, we calculate the phonon frequencies along the main symmetry directions in 2D BZ by using the PHONOPY program [35], which is based on the finite-displacement method as implemented in VASP. These calculations were performed by using (4 × 4) supercells for H and T, and (4 × 6) supercells for T' structures. The real values of the phonon mode frequencies over the whole BZ is regarded as the stability of the structures. In Fig. 2, we present the calculated phonon branches of RuX_2 compounds in the H, T, and T' structures. The acoustic branches of H and T structures have large imaginary modes at almost all directions in hexagonal BZ indicating vibrational instability. As can be seen from phonon dispersions of T' forms, there are eighteen separated branches which include three acoustical and fifteen optical branches. These nondegenerate modes show that the lattice symmetries of T-RuX_2 are broken because of the distortion. All T'-RuX_2 structures have positive phonon frequencies in the whole BZ. As X atoms get heavier, their highest optical frequencies becomes lower. As an example, at the Γ point, while RuS_2 has the highest transverse optical (TO) mode at 13.13 THz, $RuSe_2$ has a TO mode at 9.65 THz. As can be seen from Fig. 2, the longitudinal and transverse acoustical branches have linear dispersion while **k** goes to zero. On the other hand, out-of-plane ZA (transverse acoustical branch) eigenmode displays quadratic dispersion around the Γ point due to the fact that the force constants related to the transverse motion of atoms decay rapidly [47]. The ZA vibration also corresponds to the ultrasonic wave propagating with the lowest group velocity. We also present the vibrational densities of states of RuX_2. The

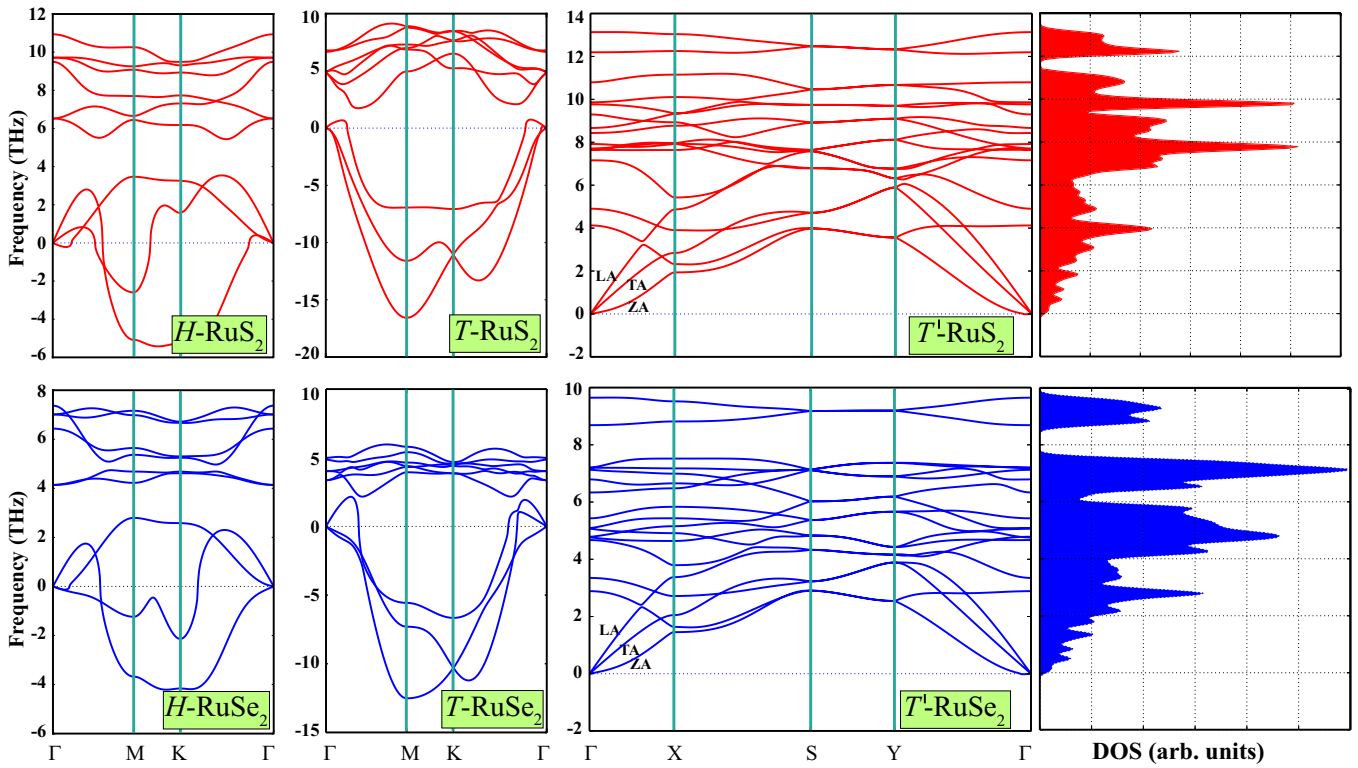

FIG. 2. *Ab initio* phonon dispersion curves of H, T, and T'-RuX_2 systems along the main symmetry directions in the 2D Brillouin zone. The vibrational density of states are also presented.

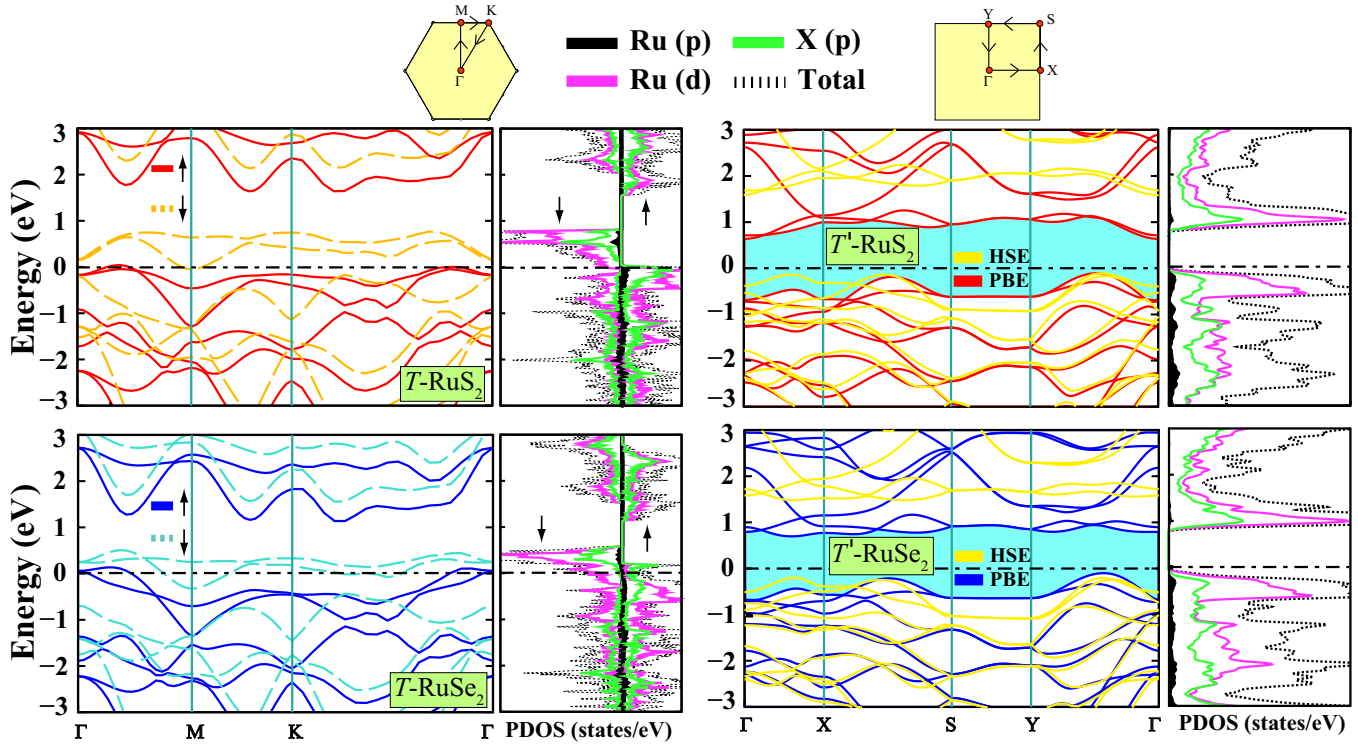

FIG. 3. The electronic band structures and the orbital projected partial electronic density of states of T and $T^{'}$ structures of RuS_2 and $RuSe_2$ systems. Two-dimensional Brillouin zones are also presented at the top side.

phonon dispersions have band gaps at various regions. The RuS_2 structure has a 0.54 THz band gap around 11.39 THz and $RuSe_2$ has a 0.90 THz band gap around 7.64 THz.

We perform molecular dynamics (MD) simulation of both RuS_2 and $RuSe_2$ systems in order to verify the structural stability at elevated temperatures. Here the structures are kept at 500 K for 2 ps. Molecular dynamics calculations are performed for 2×3 supercells of T'-RuX_2 structures. After MD, the T' structures are preserved without creation of any structural dislocations and defects as a verification of rigidness of the systems. In this case, the bond stretching is also not remarkable to induce a bond dissociation. These calculations including the phonon dispersion are the vigorous tests for the stability of the proposed structures. Furthermore, we calculate the in-plane stiffness of T'-RuX_2 structures and the results are presented in Table I. These values are smaller than 2D H-MoS_2, H-$MoSe_2$ or their W composites [12], and smaller than distorted ReS_2 [48], but comparable to or bigger than many 2D MX_2 (for X = S or Se) or silicene, germanene, and group III-V binary compounds [49].

In Fig. 3, we present 2D Brillouin zones of RuX_2 structures at the top side and the electronic band structures and partial density of states of RuS_2 and $RuSe_2$ systems (for T and T'). As seen from Fig. 3, while all T-RuX_2s have ferromagnetic metallic character with Ru d states crossing the Fermi level and a net magnetic moment, T'-RuX_2 structures show nonmagnetic semiconductor properties. A Peierls transition is also a metal-semiconductor transition [44], so this type of phase transition also occurs via Peierls distortion in the present study. T'-RuS_2 and T'-$RuSe_2$ have almost same band structures except band gaps. So, T'-RuS_2 and T'-$RuSe_2$ are suitable materials for semiconductor electronic, optoelectronic devices, and sensors with these band-gap values. Both of them have indirect band gaps as like as their bulk pyrite forms (see Supplemental Materials [41]), while their T phases are metals. T'-RuS_2 has 0.745 eV energy gap in 2D form, while it has 1.22 [50] or 1.3 eV gap [51] in bulk structure. T'-$RuSe_2$ has a 0.798 eV energy gap; this value is approximately the same as its bulk pyrite form (0.76 eV) [50]. In Fig. 3, we also present partial density of states at the right side of band structures. As seen for all the structures, the major contribution comes from Ru d orbitals and from p orbitals of X (S, Se) atoms. The relatively small contribution comes from s orbitals of X atoms at the upper part of Fermi level and Ru p orbitals

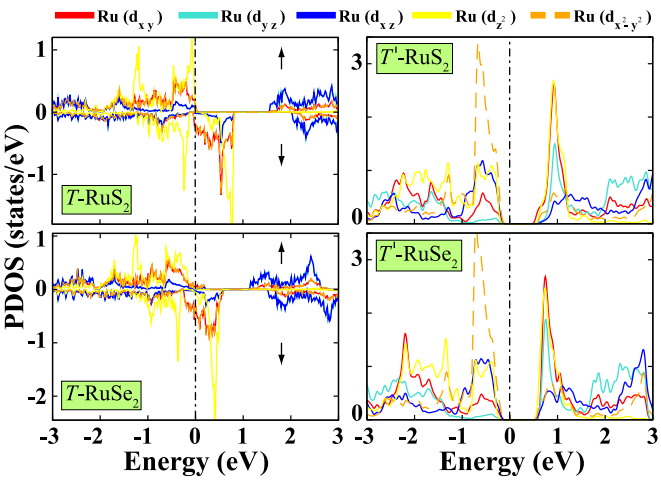

FIG. 4. d orbital projected partial electronic density of states of T and $T^{'}$ structures of RuS_2 and $RuSe_2$ systems.

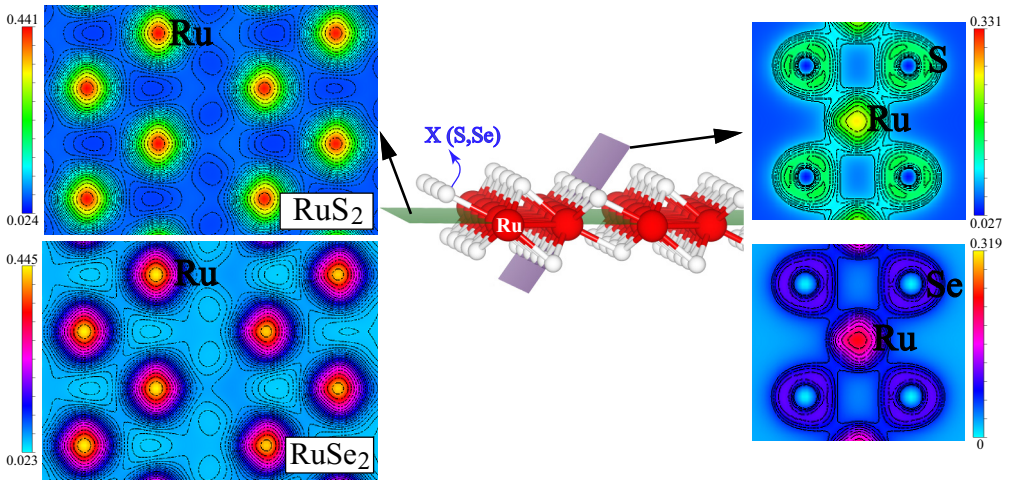

FIG. 5. Contour plots of the total charge densities of T' structures of RuS_2 and $RuSe_2$ systems.

below the Fermi level. To investigate the effects of Peierls distortion on the electronic structure of RuX_2 in detail, we plot partial Ru d orbitals in Fig. 4. While e_g (d_{z^2}, $d_{x^2-y^2}$) and t_{2g} (d_{xy}, d_{xz}, d_{yz}) orbitals give localized states at the Fermi level in T-RuX_2, the conduction bands split into two bands upon distortion. e_g orbitals split and the fully occupied $d_{x^2-y^2}$ orbital shifts to lower energies. Similarly, t_{2g} orbitals split and the major contributions around valence band maximum come from

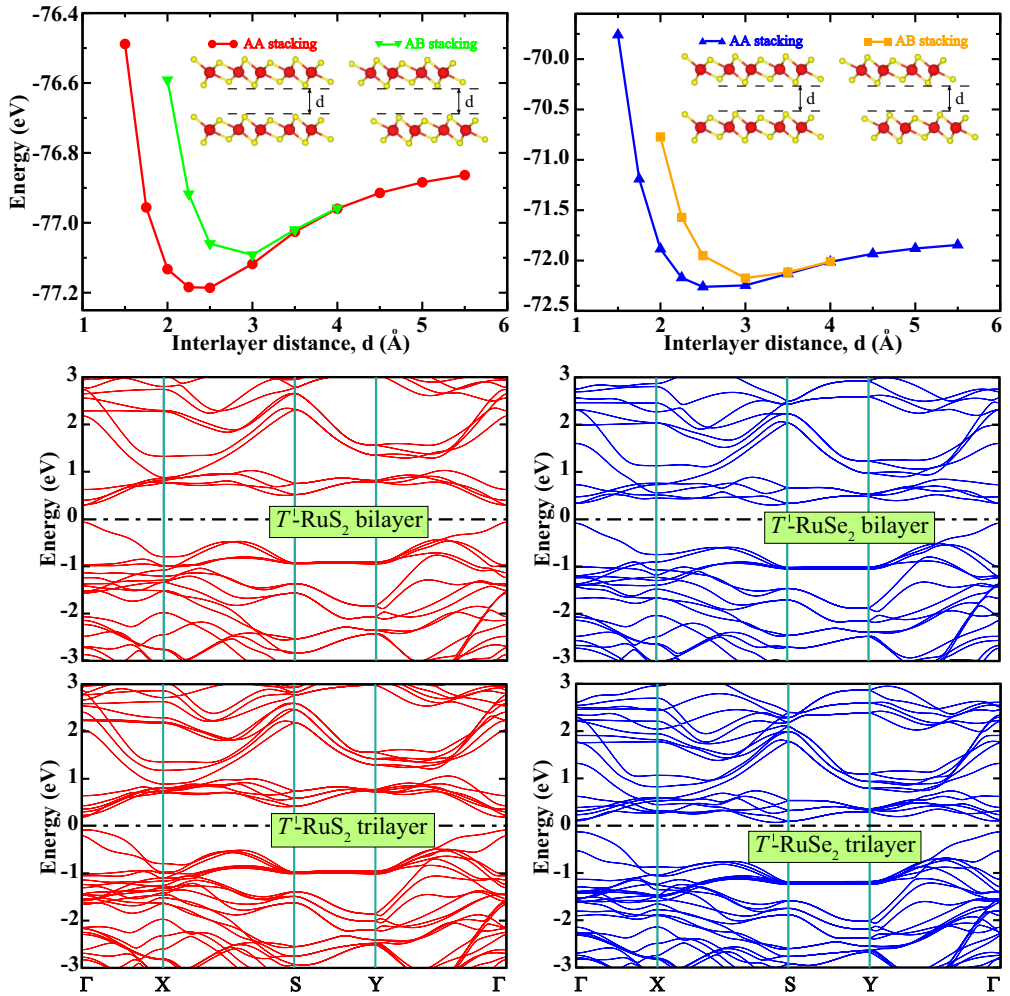

FIG. 6. T'-RuX_2 bilayer energies as a function of interlayer distance for AA- and AB-type configurations. Energy band structures for bilayer and trilayer systems are also given.

d_{xz}, while d_{xy} and d_{yz} orbitals donate the conduction-band minimum. This orbital splitting makes RuX_2 systems stable semiconductor materials.

In Fig. 5, we present the contour plots of the total charge densities for T'-RuX_2 structures together with two slicing planes labeled by the green color for the charge density of Ru chains and by the purple color for the charge density of T'-RuX_2 bonds. Ru-Ru chains have covalent-type bonding, but this bond gets weaker with increasing atomic radius (from S atom to Se atom), so Ru-Ru bond lengths extend from 2.829 Å to 2.910 Å. As mentioned earlier, Ru-S and Ru-Se bonds have covalent-type character due to the similarity of electronegativities of Ru and X atoms.

We also construct RuX_2 bilayer and trilayers to determine the effects of layer-layer interactions on electronic structure of the systems. In Fig. 6, the total energies as a function of interlayer distance are presented for two different arrangements; namely AA and AB. For both systems, AA-type stacking is energetically more favorable than other with ∼0.2 eV lower energy. The energy profile indicates a weak bonding between layers with approximately 2.4 and 2.6 Å equilibrium distances for RuS_2 and $RuSe_2$, respectively. This interlayer bonding is expected to be a van der Waals-type interaction, when both equilibrium distances and energy scales are considered. Many 2D structures turn to metal or semimetal in bilayer or multilayer forms, while being a semiconductor in their monolayer form [25,52]. Our proposed structures have direct band gaps at the Γ point for their multilayers. AA-type RuS_2 have 0.364 and 0.274 eV band gaps for bilayer and trilayer forms, respectively, while the corresponding gap values of the $RuSe_2$ system are 0.422 and 0.232 eV.

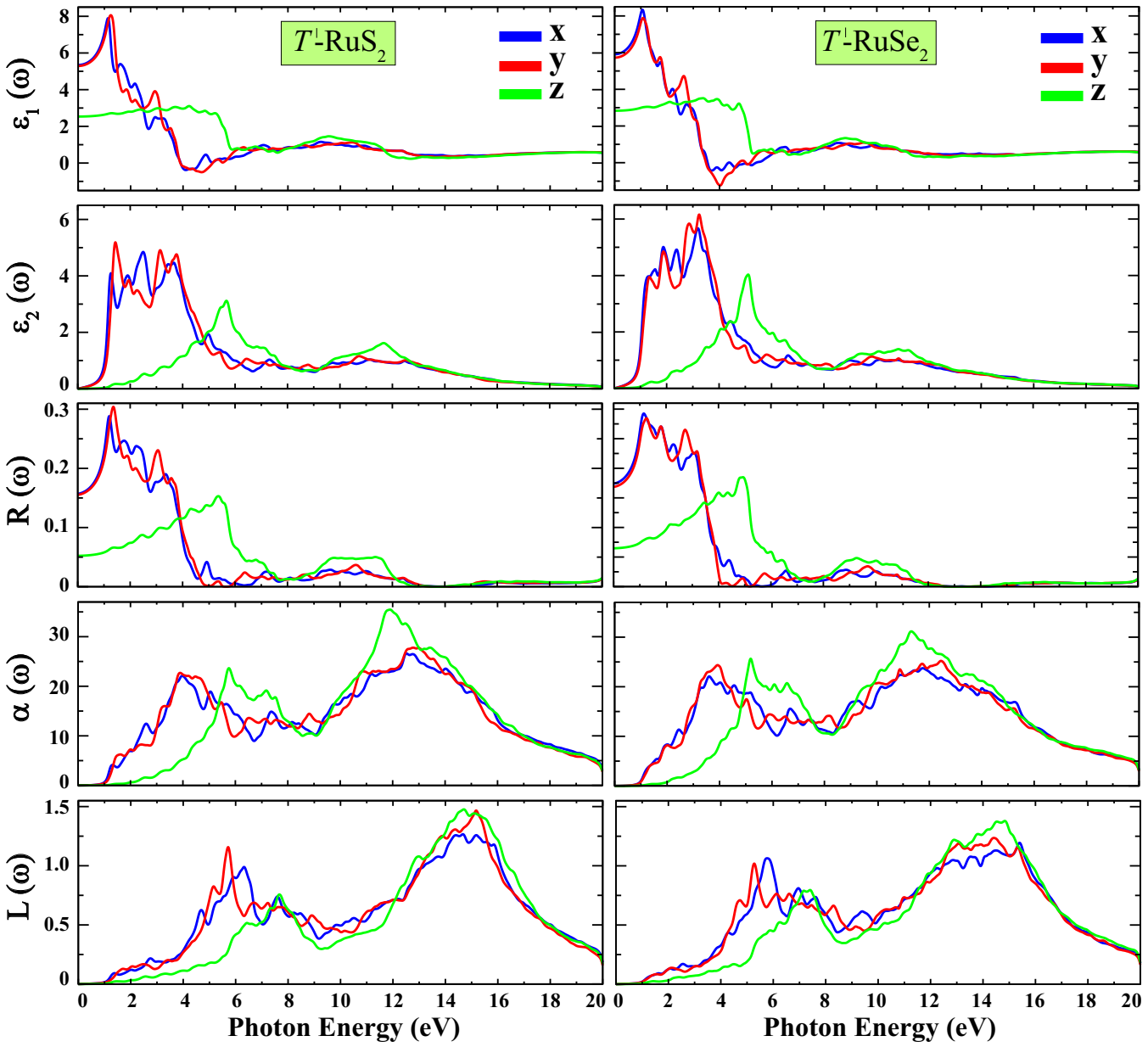

FIG. 7. Dynamical dielectric response function $\varepsilon(\omega)$, reflectivity R(ω), adsorption coefficient $\alpha(\omega)$, and energy-loss spectrum L(ω) as a function of photon energy.

The dielectric constants, Born effective charges (see Supplemental Materials for BEC [41]), and frequency-dependent dielectric matrix are calculated for all the $T^{'}$-RuX_2 structures studied, after the electronic ground states are determined. The optical properties can be estimated from the frequency-dependent dielectric function $\varepsilon(\omega)$, this dielectric function can be written in two parts as $\varepsilon(\omega) = \varepsilon_1(\omega) + i\varepsilon_2(\omega)$. The imaginary part of $\varepsilon(\omega)$ is determined by a summation over empty states and the real part of the dielectric tensor ε_1 is obtained by the usual Kramers–Kronig transformation. These methods are explained in detail by Gajdoś *et al.* [53].

Due to the anisotropic cubic cell of $T^{'}$-RuX_2, we found that the in-plane static dielectric constants ϵ_{xx} and ϵ_{yy} are not equal. The calculated values of ϵ_{xx} is 4.87 and 5.51 while ϵ_{yy} is 5.17 and 5.62 for $T^{'}$-RuS_2 and $T^{'}$-$RuSe_2$, respectively. These values are independent of the vacuum separation used in the calculation. However, the out-of-plane dielectric constant converges to zero as the vacuum separation is increased. Instead, we calculated the 2D polarizability $\alpha_{2D} = \lim_{L\to\infty}(\epsilon_\perp - 1)L$ where L is the vacuum separation [54]. The values for the 2D polarizability were found to be 1.02 and 1.05 for $T^{'}$-RuS_2 and $T^{'}$-$RuSe_2$, respectively. The dielectric constants obtained are at least ∼35 % lower than that of monolayer Mo(W)X_2 (X = S, Se) [55].

In Fig. 7, we present the frequency-dependent real and imaginary part of the dielectric function and the linear optical spectral quantities for $T^{'}$-RuX_2 structures. We also give the required equations to calculate these properties in the Supplemental Materials [41]. When we consider the imaginary parts of dielectric functions and electronic partial density of states for both $T^{'}$-RuX_2 structures, we can see that interior intra-optical excitations occur between the valence bands (VBs) and conduction bands (CBs). For $T^{'}$-RuS_2, the threshold energy of $\varepsilon_2(\omega)$ is about 0.8 eV, which is similar for $T^{'}$-$RuSe_2$. The first peak of the spectrum is situated around 1.4 and 1.9 eV for $T^{'}$-RuS_2 and $T^{'}$-$RuSe_2$, respectively. These energy values are attributed to the interband transitions from Ru d orbitals in the VB maximum to Ru d and X p (X = S, Se) orbitals in the CB minimum. Other peaks of $\varepsilon_2(\omega)$ in the range of 2–6 eV come from the excitations between the Ru p and d and X p states in the VB to Ru d and X p states in the CB for both $T^{'}$ structures. As seen in Fig. 7, the reflectivity spectra of $T^{'}$-RuX_2 structures have intensity peaks in the range of 1–4 eV, which means that the systems cannot be good optically transparent materials in the visible region, but according to the spectra they can be transparent in the UV range. In contrast with high reflectivity, they exhibit lower absorption under 1.0 eV and the onsets of $T^{'}$-RuX_2 appear after 1.0 eV. The maximum peaks in the absorption spectra appear at 11.9 and 11.2 eV for $T^{'}$-RuS_2 and $T^{'}$-$RuSe_2$, respectively. On the other hand, both structures show relatively good absorbance to use in photovoltaic applications. L(ω) energy-loss spectrum can demonstrate the collective excitations. From Fig. 7, we see the two maxima which are occur at 5.9 and 15 eV for $T^{'}$-RuS_2 and 5.3 and 14.7 eV for $T^{'}$-$RuSe_2$. These values indicate the plasmon resonances.

As a final remark, we note that the excitonic effects are not included in calculations. Excitons, which are tightly bound electron-hole pairs, can have remarkable effects in the optoelectronic spectra of the various semiconducting systems. It was reported that excitons can have ≈0.55 eV binding energy for monolayer $MoSe_2$ on graphene [56–58]. The strong interactions of excitons with electromagnetic fields can alter the optical behavior of these materials. This phenomenon is able to bring new perspectives to the optoelectronics of semiconducting monolayer TMD systems including the proposed systems in this study.

IV. CONCLUSIONS

In summary, with our first-principles calculations, we predict two different and new individual components of the MX_2 family. The phonon-frequency calculations indicate that distorted RuX_2 (X = S, and Se) structures in $T^{'}$ form can remain stable as free-standing structures. The stability is confirmed by molecular dynamics simulation at elevated temperatures. We hope that these analysis can be an incentive for experimentalists to exfoliate 2D RuS_2 or $RuSe_2$ systems. From the technological point of view, their semiconductor band gaps are very suitable for applications in electronic, optoelectronic, and sensor technology.

ACKNOWLEDGMENTS

Computing resources used in this work were provided by the TUBITAK ULAKBIM, High Performance and Grid Computing Center (Tr-Grid e-Infrastructure). S.C. acknowledges support from The Scientific and Technological Research Council of Turkey (TUBITAK) under the project number 115F388. A.R. acknowledges financial support from the European Research Council (ERC-2015-AdG-694097), Spanish grant (FIS2013-46159-C3-1-P), Grupos Consolidados (IT578-13), and AFOSR Grant No. FA2386-15-1-0006 AOARD 144088, H2020-NMP-2014 project MOSTOPHOS (GA No. 646259) and COST Action MP1306 (EUSpec).

[1] K. S. Novoselov *et al.*, Science **306**, 666 (2004).
[2] A. K. Geim and K. S. Novoselov, Nat. Mater. **6**, 183 (2007).
[3] S. Cahangirov, M. Topsakal, E. Akturk, H. Sahin, and S. Ciraci, Phys. Rev. Lett. **102**, 236804 (2009).
[4] D. Pacile *et al.*, Appl. Phys. Lett. **92**, 133107 (2008).
[5] X. Song, J. Hu, and H. Zeng, J. Mater. Chem. C **1**, 2952 (2013).
[6] F. Ersan, G. Gokoglu, and E. Akturk, Appl. Surf. Sci. **303**, 306 (2014).
[7] Q. Peng *et al.*, Comput. Mater. Sci. **68**, 320 (2013).
[8] C. W. Zhang *et al.*, Chem. Phys. Lett. **548**, 60 (2012).
[9] J. Li, N. V. Medhekar, and V. B. Shenay, J. Phys. Chem. C **117**, 15842 (2013).
[10] H. Guo *et al.*, J. Phys. Chem. C **118**, 7242 (2014).
[11] G. Cunningham *et al.*, ACS Nano **6**, 3468 (2012).
[12] C. Ataca, H. Sahin, and S. Ciraci, J. Phys. Chem. C **116**, 8983 (2012).

[13] H. P. Komsa and A. V. Krasheninnikov, J. Phys. Chem. Lett. **3**, 3652 (2012).
[14] S. Tongay *et al.*, Nat. Commun. **5**, 3252 (2014).
[15] F. A. Rasmussen and K. S. Thygesen, J. Phys. Chem. C **119**, 13169 (2015).
[16] J. A. Wilson and A. D. Yoffe, Adv. Phys. **18**, 193 (1969).
[17] A. D. Yoffe, Annu. Rev. Mater. Sci. **3**, 147 (1973).
[18] H. L. Zhuang *et al.*, Appl. Phys. Lett. **104**, 022116 (2014).
[19] A. Kuc, N. Zibouche, and T. Heine, Phys. Rev. B **83**, 245213 (2011).
[20] H. Zeng *et al.*, Nat. Nanotechnol. **7**, 490 (2012).
[21] K. F. Mak *et al.*, Nat. Nanotechnol. **7**, 494 (2012).
[22] S. Bertolazzi, J. Brivio, and A. Kis, ACS Nano **5**, 9703 (2011).
[23] H. Li *et al.*, Small **9**, 1974 (2013).
[24] M. Chhowalla *et al.*, Nat. Chem. **5**, 263 (2013).
[25] M. Ghorbani-Asl, A. Kuc, P. Mir, and T. Heine, Adv. Mater. **28**, 853 (2015).
[26] H. I. Lee and J. M. White, J. Catal. **63**, 261 (1980).
[27] N. W. Cant, P. C. Hicks, and B. S. Lennon, J. Catal. **54**, 372 (1978).
[28] H. Over *et al.*, Science **287**, 1474 (2000).
[29] T. A. Pecoraro and R. R. Chianelli, J. Catal. **67**, 430 (1981).
[30] H. M. Kuhne and H. Tributsch, J. Electrochem. Soc. **130**, 1448 (1983).
[31] S. R. Svendsen *et al.*, J. Chem. Thermodyn. **19**, 1009 (1987).
[32] P. E. Blöchl, Phys. Rev. B **50**, 17953 (1994).
[33] G. Kresse and J. Furthmuller, Phys. Rev. B **54**, 11169 (1996).
[34] J. P. Perdew, K. Burke, and M. Ernzerhof, Phys. Rev. Lett. **77**, 3865 (1996).
[35] A. Togo and I. Tanaka, Scr. Mater. **108**, 1 (2015).
[36] H. J. Monkhorst and J. D. Pack, Phys. Rev. B **13**, 5188 (1976).
[37] J. Heyd, G. E. Scuseria, and M. Ernzerhof, J. Chem. Phys. **118**, 8207 (2003).
[38] A. V. Krukau, O. A. Vydrov, A. F. Izmaylov, and G. E. Scuseria, J. Chem. Phys. **125**, 224106 (2006).
[39] P. Mori-Sánchez, A. J. Cohen, and W. Yang, Phys. Rev. Lett. **100**, 146401 (2008).
[40] S. Grimme, J. Comput. Chem. **27**, 1787 (2006).
[41] See Supplemental Material at http://link.aps.org/supplemental/10.1103/PhysRevB.94.155415 for the calculated structural parameters of bulk pyrite form, the electronic band structures of RuX_2 using different methods, some crystallographic data regarding 2D RuX_2, thermodynamic properties, and Born effective charge tensors.
[42] M. Calandra, Phys. Rev. B **88**, 245428 (2013).
[43] D. H. Keum *et al.*, Nat. Phys. **11**, 482 (2015).
[44] I. B. Bersuker, *The Jahn Teller Effect* (Cambridge University Press, Cambridge, UK, 2006).
[45] G. Henkelman, A. Arnaldsson, and H. Jonsson, Comput. Mater. Sci. **36**, 354 (2006).
[46] M. Topsakal, S. Cahangirov, and S. Ciraci, Appl. Phys. Lett. **96**, 091912 (2010).
[47] F. Liu, P. Ming, and J. Li, Phys. Rev. B **76**, 064120 (2007).
[48] Z. G. Yu, Y. Cai, and Y. W. Zhang, Sci. Rep. **5**, 13783 (2015).
[49] H. Şahin *et al.*, Phys. Rev. B **80**, 155453 (2009).
[50] H. P. Vaterlaus *et al.*, J. Phys. C: Solid State Phys. **18**, 6063 (1985).
[51] R. Bichsel, F. Levy, and H. Berger, J. Phys. C: Solid State Phys. **17**, L19 (1984).
[52] S. Zhang, Z. Yan, Y. Li, Z. Chen, and H. Zeng, Angew. Chem. **127**, 3155 (2015).
[53] M. Gajdoś, K. Hummer, G. Kresse, J. Furthmüller, and F. Bechstedt, Phys. Rev. B **73**, 045112 (2006).
[54] P. Cudazzo, I. V. Tokatly, and A. Rubio, Phys. Rev. B **84**, 085406 (2011).
[55] R. K. Ghosh and S. Mahapatra, IEEE J. Electron Devices Soc. **1**, 175 (2013).
[56] M. M. Ugeda, A. J. Bradley, S.-F. Shi, F. H. da Jornada, Y. Zhang, D. Y. Qiu, W. Ruan, S.-K. Mo, Z. Hussain, Z.-X. Shen, F. Wang, S. G. Louie, and M. F. Crommie, Nat. Mater. **13**, 1091 (2014).
[57] Z. S. Wu *et al.*, Adv. Funct. Mater. **20**, 3595 (2010).
[58] L. Van Hove, Phys. Rev. **89**, 1189 (1953).